Post-CMOS Compatible Aluminum Nitride MEMS Filters and Resonant Sensors

Roy H. Olsson III, James G. Fleming, Kenneth E. Wojciechowski, Michael S. Baker, and Melanie R. Tuck
Advanced MEMS Department
Sandia National Laboratories
Albuquerque, USA
rholsso@sandia.gov

Abstract—**This paper reports post-CMOS compatible aluminum nitride (AlN) MEMS resonators, filters, and resonant sensors for the miniaturization of radio-frequency transceivers and sensor systems. Utilizing a resonator with two closely spaced modes, 2nd order MEMS filters occupying 0.06 mm^2 have been realized in a single device. Methods for tuning the bandwidth and center frequency of these filters lithographically have been demonstrated. A 0.5% bandwidth, 108.4 MHz dual mode filter has a measured insertion loss of 9.4 dB with 50 Ω termination which can be reduced to 4.7 dB by terminating the filter with 75 Ω. In order to scale MEMS resonators to higher frequencies without increasing the size or impedance, resonators selectively driven at a harmonic determined by interdigitated drive and sense electrodes have been demonstrated reaching frequencies of 796 MHz with impedances of approximately 100 Ω and quality factors in excess of 750 in air. In the same process resonant sensors based on AlN double-ended tuning fork (DETF) sensing beams have been demonstrated at 727 kHz with quality factors of 2160. An oscillator based on the DETF sensing beams achieves a phase noise of -81 dBc/Hz at 275 Hz offset from the carrier. A 100 ng mass coupled to a pair of DETF sensors achieves an acceleration sensitivity of 565mG/√Hz for accelerations from 275 to 1100 Hz.**

I. Introduction

There is increasing demand to decrease size, reduce packaging overhead, and expand capabilities in radio-frequency (RF) circuits, sensors, and microsystems. In consumer RF the desire for low cost, small transceivers has lead to the development of low-IF and zero-IF radio architectures [1] that utilize a minimum number of high-Q off-chip components, typically a quartz crystal and an RF filter. The lack of high-Q filtering leads to poor sensitivity, image rejection and dynamic range when compared to the superheterodyne transceiver. While the relatively poor performance of low-IF and zero-IF transceivers is acceptable in most consumer applications, in many non-consumer applications it is not. Still, there is large demand for the miniaturization of radios in non-consumer applications without sacrificing the sensitivity and immunity to interferers associated with traditional superheterodyne transceivers.

Miniaturization is also of great interest in the area of sensors. Integration of readout electronics with sensors on the same substrate not only reduces size but generally improves performance. Further size reductions can be obtained through the integration of sensors with communications circuitry and devices. When integrating either RF MEMS communication devices such as filters and resonators or MEMS sensors (inertial, chemical, biological) with CMOS circuitry it is highly desirable to have the MEMS devices processed post-CMOS. In this way RF MEMS and MEMS sensors can be realized directly on top of the most advanced CMOS circuitry.

This paper reports the development of post-CMOS compatible aluminum nitride (AlN) MEMS devices for the miniaturization of high performance radios and sensors. The AlN fabrication process allows for the realization of resonators, filters, and resonant sensors operating over the frequency range from 500 kHz to in excess of 1 GHz. By utilizing a novel AlN resonator with two closely spaced high quality factor (≈ 1000 in air) modes, a 108.4 MHz, 0.5% bandwidth filter has been realized in a single device occupying only 0.06 mm^2 of die space. This filter has an impedance of 100 Ω, a 1 dB compression point of 7 dBm, a 20 dB shape factor of 2.3, and a stop band rejection of 55 dB. Both the operating frequency and bandwidth of the dual mode filter are lithographically definable and banks of these filters covering the frequency range from 106 – 113 MHz for advanced radios have been realized. Resonators selectively driven at the 5th, 6th, and 7th harmonic have been developed to allow the scaling of AlN resonators to higher frequencies without subsequent increases in the resonator size or impedance. Such devices have achieved a maximum operating frequency of 796 MHz and impedances as low as 96 Ω while retaining high quality factors in excess of 750 in air. Resonant accelerometers based on piezoelectrically driven, double-ended tuning fork (DETF) resonators have also been developed in this AlN process. An accelerometer based on 727 kHz oscillating beams occupies 0.15 mm^2 of die space

This work was supported by the Laboratory Directed Research and Development (LDRD) program at Sandia National Laboratories. Sandia National Laboratories is a multiprogram laboratory operated by the Sandia Corporation, Lockheed Martin Company, for the United States Department of Energy's National Nuclear Security Administration under contract DE-AC04-94AL85000.

and has a sensitivity of 565mG/√Hz for vibrations from 275 to 1100 Hz.

II. Aluminum Nitride Device Transduction and Fabrication

A. Piezoelectric Resonator Transduction

It is widely known that piezoelectric materials such as AlN can be used to drive and sense acoustic devices. Until recently most MEMS resonators were transduced electrostatically via small capacitive gaps [2] due to the lack of available processes for micromachining piezoelectric thin films. Recently, leveraging many of the processes developed for manufacturing AlN film bulk acoustic resonators (FBARs) [3], a method for fabricating lithographically definable, piezoelectrically driven, AlN MEMS resonators has been developed [4]. Piezoelectric resonator actuation has three main advantages over traditional electrostatic transduction. First, piezoelectric actuation has orders of magnitude higher electro-mechanical coupling than capacitive actuation. This results in much lower impedances for piezoelectrically driven devices. Second, the force on a piezoelectric actuator is linear with drive voltage while capacitive actuator force goes as the square of the drive voltage. Thus, the power handling of piezoelectric resonators is orders of magnitude higher than similar devices transduced electrostatically. While the gaps of capacitively transduced resonators can be filled with high dielectric constant materials to reduce the impedance [5], this does not improve the dynamic range because of a subsequent drop in power handling and results in large transducer capacitance which can exceed 15 pF. Finally, piezoelectric transduction does not require a bias voltage which often exceeds 10 volts for capacitively transduced resonators [6]. The only apparent drawback to piezoelectric transduction is the reduced quality factor of the materials used to realize the resonator which typically limits the Q to a few thousand compared to greater than 100,000 for electrostatically transduced silicon devices [2]. Despite these high-Q values the application of capacitively transduced filters has been significantly limited because of the high impedance and low power handling. In resonant sensors the 4.6x reduction in Q between capacitively [7] and piezoelectrically driven resonant sensing beams is offset by the improved power handling of the piezoelectric resonators, resulting in lower oscillator phase noise and improved sensor sensitivity over a wider bandwidth.

B. Fabrication

The process flow used to fabricate the AlN resonators, filters and sensors is shown in Fig. 1. The process replaces the platinum bottom electrode in [4] with standard CMOS metals, aluminum (Al), titanium (Ti), titanium nitride (TiN) and tungsten (W). (a) The process begins with an anisotropic silicon (Si) etch and the deposition of a silicon dioxide (SiO_2) layer to isolate the bottom electrode from the substrate. Tungsten is then deposited by chemical vapor deposition (CVD) and chemically mechanically polished (CMP) until it remains only where Si was etched. An oxide touch polish is then performed to further smooth the wafer surface prior to the sputter deposition and patterning of the bottom electrode. Two separate bottom electrode processes have been developed, one with a 50 nm Al bottom electrode and a more recently developed process utilizing a Ti(20 nm)/TiN(50 nm)/Al(50 nm) bottom electrode. Next, 750 nm of AlN is sputter deposited at 350 °C. Using this process highly oriented c-axis AlN films necessary for realizing low impedance resonators can be reliably formed. Typical rocking curve full width half maximum values for the AlN film measured using X-ray diffraction are 3.1° on Al and 1.5° on Ti/TiN/Al. Resonators realized using the more highly oriented AlN on Ti/TiN/Al exhibit 2.25 times lower impedance when compared to identical resonators on an Al bottom electrode. (b) Contacts to the W areas are etched in the AlN and a 100 nm thick Al top electrode is deposited and patterned. (c) Finally, the resonator frequency is lithographically defined by etching trenches in the AlN and SiO_2 to bulk Si and the devices are released using an isotropic etch in dry SF_6 or XeF_2. The maximum temperature in this process is 350 °C and all of the materials are post-CMOS compatible and can be deposited and etched using standard CMOS tools.

III. Dual Mode Aluminum Nitride Filter Banks

Small size is a key property driving the pursuit of microresonator based filters to replace current technologies such as surface acoustic wave (SAW) and quartz filters. The small microresonator footprint leads not simply to radio miniaturization but also enables large banks of filters to be integrated on the same substrate, allowing multi-channel radios or real time spectral analysis on a single chip. A dual mode filter, that implements a 2nd order band-pass filter using a single resonator for reduced size, has been developed and is pictured with critical filter dimensions in Fig. 2. An SEM image of the dual mode filter is shown in Fig. 3. The dual mode filter operates by closely spacing the frequencies of two resonant modes in a single device. While dual mode filters have been previously reported at lower frequencies [8], this filter utilizes the mode shapes shown in Fig. 4, which are more

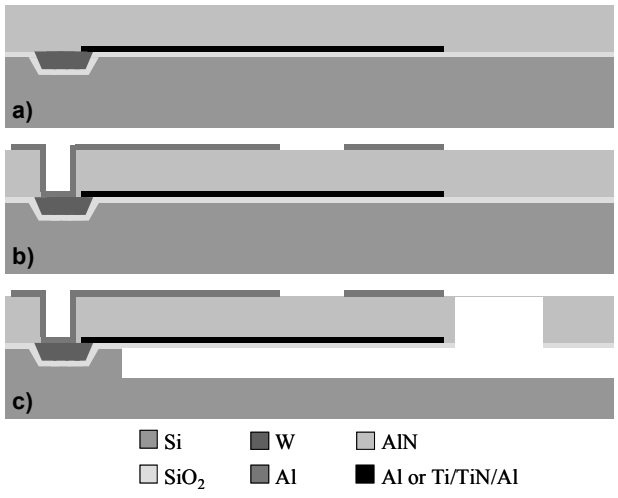

Figure 1. Aluminum nitride microfilter and sensor fabrication process.

suitable for realizing low impedance filters at frequencies in excess of 100 MHz. A time varying voltage applied across the AlN film on the drive electrode causes the drive half of the ring to expand and contract in-plane due to the d_{31} piezoelectric coefficient. *Mode 0* represents the mode shape where the sense half of the ring vibrates out of phase with the drive while *mode 1* is the mode shape where the drive and sense halves of the ring vibrate in phase. The output is a time varying current at the sense electrode due to the d_{31} piezoelectric coefficient. The bottom electrode is grounded in this configuration which significantly reduces the feedthrough capacitance between the drive and sense electrodes, vastly increasing the filter stopband rejection. The dual mode filter is a reciprocal device allowing the drive and sense electrodes to be interchanged. The filter passband is located at approximately

$$f_{FILTER} \approx \frac{1}{2W}\sqrt{\frac{E}{\rho}} \quad (1)$$

where W is the width of the ring shown in Fig. 2 and E and ρ are the effective Young's modulus (225 GPa) and density (2956 kg/m^3) of the resonator film stack. The resonant frequency for both modes of a dual mode filter with ring width, $W = 41\ \mu m$, vs. filter width to radius ratio, R/W, are shown in Fig. 5. Increasing the radius of the filter decreases the resonant frequency for both modes but at a different rate, allowing the filter bandwidth and center frequency to be independently set by adjusting W and R. The devices explored in this work have resonant frequencies between 106 – 113 MHz and % mode separations between 0.3 and 0.6 %. The design is completed by anchoring the dual mode filter using notched supports in the middle of the ring which is a nodal point of zero displacement using beams sized to be an odd multiple of a quarter wavelength for both compression and flexural modes. Using this anchoring scheme minimizes acoustic losses to the substrate.

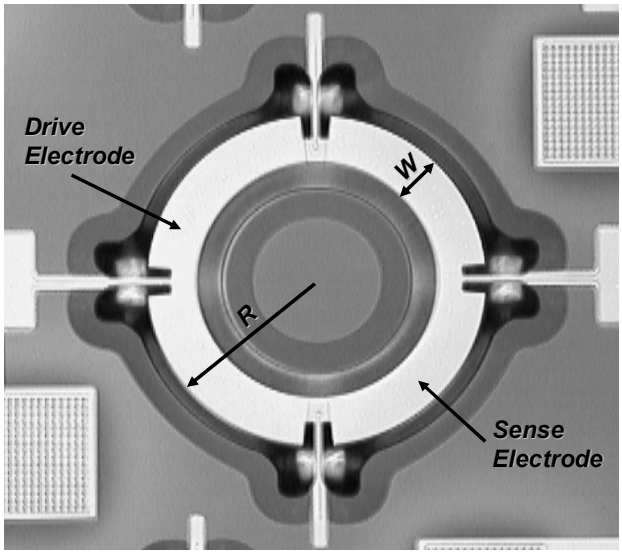

Figure 2. Picture of an AlN dual mode filter. W is 41 μm and R is 140 μm.

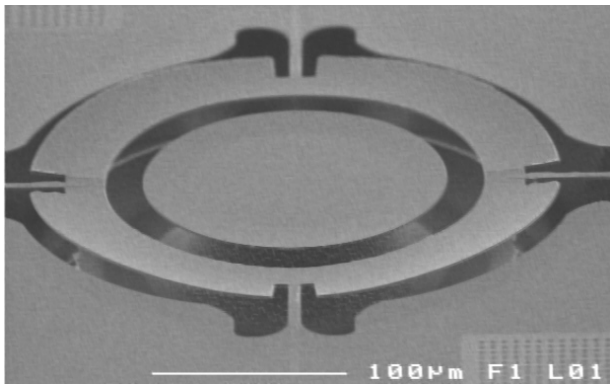

Figure 3. SEM image of the AlN dual mode filter pictured in Fig. 2.

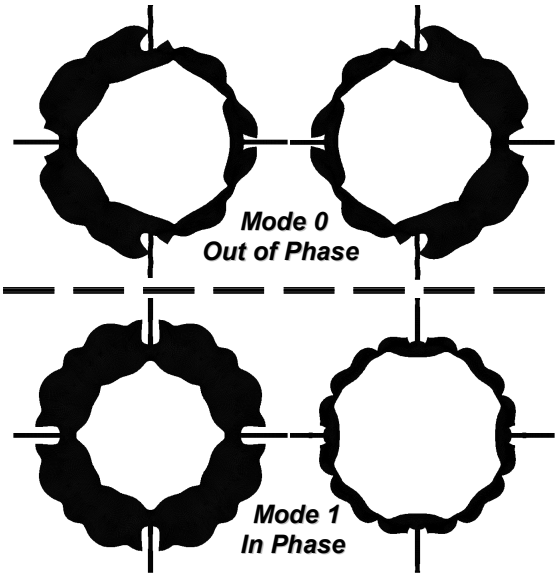

Figure 4. Image of the mode shapes used to realize the dual mode filter generated by ANSYS, a finite element modeling tool.

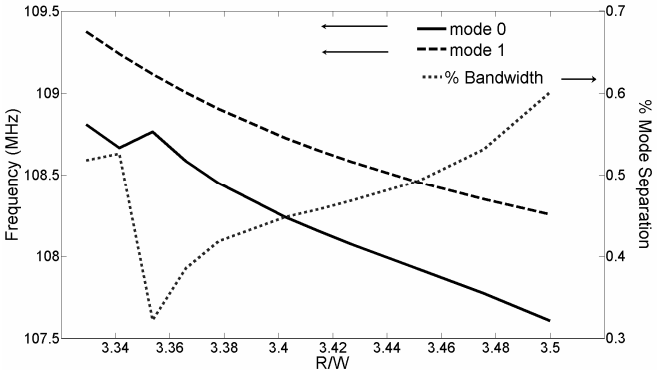

Figure 5. Frequency of the two modes in Fig. 4 for a dual mode filter with $W = 41\ \mu m$ vs. R/W. The % separation between the modes can be adjusted to control the % bandwidth of the filter.

The measured transmission (S21) in air of the dual mode filter (Ti/TiN/Al bottom electrode) with a 50 Ω source and load impedance is shown over a wide frequency span in Fig. 6 and over a narrow frequency span in Fig. 7 along with the response of an equivalent circuit model, depicted in Fig. 8, that was generated for this device. The dimensions of the filter are given in Table I, where this device is labeled as *filter0*, while the equivalent circuit values are summarized in Table II. The filter has a measured center frequency of 108.4 MHz, a 3 dB bandwidth of 560 kHz, a stopband rejection 55 dB and a 1 dB compression point of 7 dBm. The measured filter insertion loss (IL) of 9.4 dB and passband ripple (PBR) of 4.6 dB are due to the mismatch between the 100 Ω impedance of the filter and the 50 Ω termination. While this 100 Ω filter could be matched to 50 Ω using an on chip LC network, operating at a slightly higher impedance, such as 75 Ω, reduces the IL and PBR to 4.7 dB and 1 dB respectfully. The frequency response of the dual mode filter equivalent circuit model simulated with 75 Ω and 100 Ω termination impedances is shown in Fig. 7 and the filter specifications operating with different termination impedances are summarized in Table III. The dual mode filter achieves smaller size, lower insertion loss, and higher stop band rejection than previously reported contour-mode AlN ladder filters at similar frequencies terminated with kΩ impedances [9].

Five-element banks of dual mode filters have been developed to begin exploring multi-channel radios enabled by the small filter size and single substrate integration. The measured transmission (S21) of a 5-element filter bank over frequency with 50 Ω termination is shown in Fig. 9 with the dimensions of each filter summarized in Table I. *Filter1* has the same width, *W*, as *filter0* while *filter3* has the same radius, *R*. However, the ratio, *R/W*, is larger for *filters 1-5* when compared to *filter0* resulting in an increased filter bandwidth.

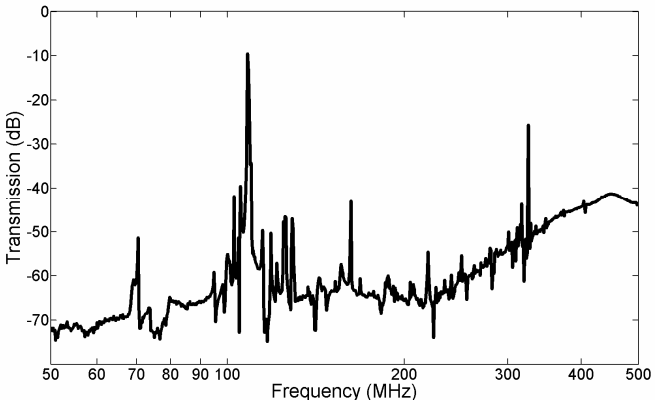

Figure 6. Measured transmission (S21) for the dual mode filter shown in Fig. 2 from 50 to 500 MHz. The stopband rejection is 55 dB and the spurious resonances are rejected by > 30 dB except for the filter 3rd harmonic.

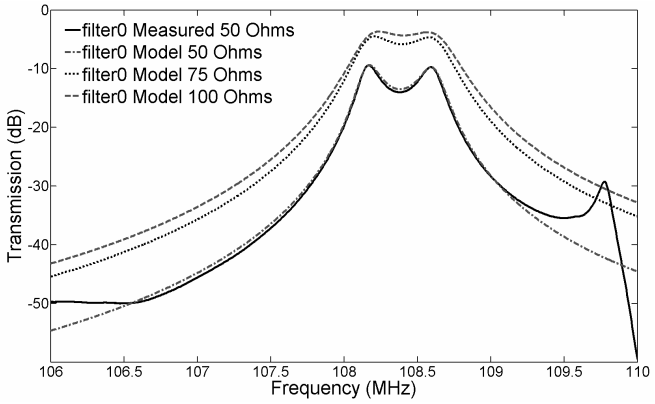

Figure 7. Measured transmission (S21) of the dual mode filter, *filter0*, along with the simulated response of the dual mode filter equivalent circuit model operating at different termination impedances.

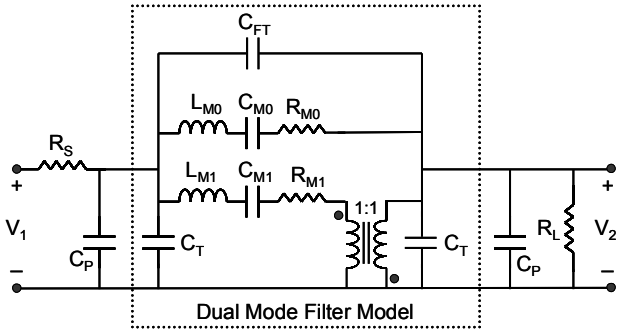

Figure 8. Equivalent circuit model of the dual mode filter. All of the circuit elements inside the dashed line are inherient to the filter including the transducer capacitors, C_T. The transformer capturers the 180° phase inversion from *mode 1*.

TABLE I. DUAL MODE FILTER DIMENSIONS AND MEASURED MODE FREQUENICES

Device	W (μm)	R (μm)	Mode 0 (MHz)	Mode 1 (MHz)	Mode Spacing (kHz)
Filter0	41	140	108.17	108.59	420
Filter1	41	143.5	106.57	107.21	640
Filter2	40.5	141.75	107.93	108.61	680
Filter3	40	140	109.37	109.97	600
Filter4	39.5	138.25	110.52	111.16	640
Filter5	39	136.5	112.09	112.77	680

TABLE II. DUAL MODE FILTER EQUIVALENT CIRCUIT PARAMATERS

Circuit Element	Value
L_{M0}	151.41 μH
C_{M0}	14.302 fF
R_{M0}	98 Ω
L_{M1}	143.65 μH
C_{M1}	14.949 fF
R_{M1}	103 Ω
C_{FT}	8.8 fF
C_T	1.85 pF
C_P	1.78 pF

TABLE III. DUAL MODE FILTER PERFORMACE FOR DIFFERENT TERMINATION IMPEDANCES

Termination Impedance	Center Frequency (MHz)	Insertion Loss (dB)	3 dB Bandwidth (kHz)	Passband Ripple (dB)	20 dB Shape Factor (dB)	Stopband Rejection (dB)	1 dB Compression (dBm)
50 Ω (measured)	108.4	9.4	560	4.6	2.27	55	7
50 Ω (model)	108.4	9.4	560	2.3	2.27	-	-
75 Ω (model)	108.4	4.7	620	1	2.6	-	-
100 Ω (model)	108.4	3.7	625	0.7	2.76	-	-

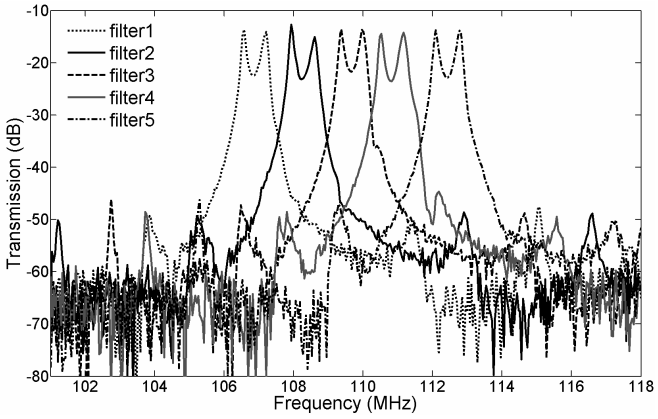

Figure 9. Response of a 5-element dual mode AlN filter bank realized on a single die.

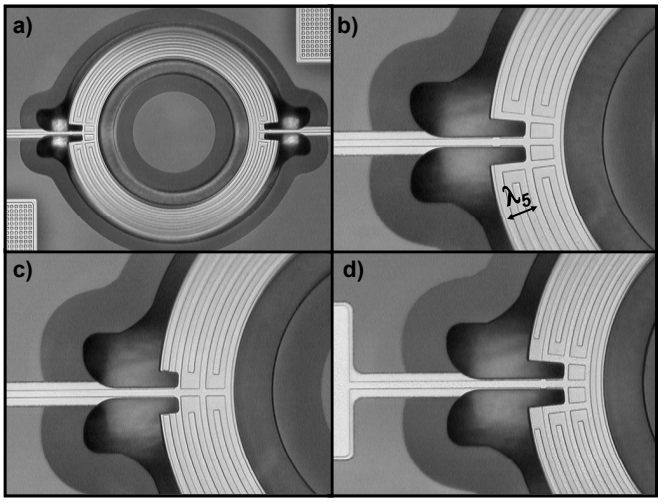

Figure 10. a) AlN resonator with interdigitated electrodes for selectively transducing the 5th harmonic. b-d) Close in image of electrodes and anchoring for 5th (b), 6th (c) and 7th (d) harmoinc resonators.

IV. HIGH FREQUENCY RESONATORS WITH INTERDIGITATED TRANSDUCTION

The impedance of the dual mode filter in Fig. 2 is proportional to resonator ring area [4]. From (1), the width, *W*, must be decreased to scale the resonator to higher frequencies, requiring a subsequent increase in ring radius, *R*, to maintain constant impedance. This can lead to a large ring radius in excess of 1 mm at GHz frequencies that negates the size advantages of MEMS filters over technologies such as SAW. A picture of an AlN resonator with interdigitated electrodes designed to selectively drive and sense the 5th resonator harmonic is shown in Fig. 10(a), with close up images of the electrodes and anchoring for 5th, 6th, and 7th harmonic interdigitated resonators shown in Fig. 10(b-d). Each of the resonators in Fig. 10 has the same width, $W = 40\,\mu m$, and radius, $R = 140\,\mu m$, corresponding to the fundamental mode at wavelength ($n = 1$)

$$\lambda_n = \frac{2W}{n}\ , \tag{2}$$

which is *mode 1* in Fig. 4. Harmonics occur at integer multiples of *n* with corresponding frequencies

$$f_n \approx \frac{\sqrt{E/\rho}}{\lambda_n}\ . \tag{3}$$

Interdigitated Al electrodes can be patterned on top of the resonator to selectively transduce a harmonic defined by the electrode location, width, and spacing. To selectively drive a harmonic the electrodes are placed at locations of maximum strain which correspond to locations of zero displacement. Since the displacement is maximized at the outer and inner edge of the ring, electrodes are centered at $\lambda_n/4$ in from the resonator edge where the maximum strain is transduced. These electrodes have a width of $\lambda_n/4$ and electrically connected electrodes are spaced λ_n apart. The drive and sense electrodes are interdigitated with a spacing between drive and sense of $\lambda_n/2$. For even order harmonics the anchoring must be changed to retain high-Q because the expansion and contraction of the outer edge of the ring is out of phase with the inner edge. Thus, the center of the ring is no longer a node of zero displacement and the anchors should be moved to such a location as seen for the 6th harmonic device in Fig. 10. The length of the anchoring supports must also be resized to an odd multiple of $\lambda/4$ for even order harmonic resonators.

The measured transmission (S21) for the resonators in Fig. 10 is shown over a 900 MHz span in Fig. 11 and in a narrower span in Fig. 12. The peak transmission corresponds to 580, 693, and 796 MHz for the 5th, 6th, and 7th harmonic resonators. The interdigitated transduction rejects all other resonator harmonics by greater than 20 dB. The impedances of the 5th, 6th and 7th harmonic resonators are 96, 96 and 140 Ω with corresponding quality factors of 774, 770, and 460. These impedance values are very close to the impedance of the similarly sized resonator in Fig. 2 operating in its fundamental mode, 103 Ω. The spurious resonances near the peak are believed to be due to the anchoring of the resonators. Experimental results with fundamental mode resonators, see

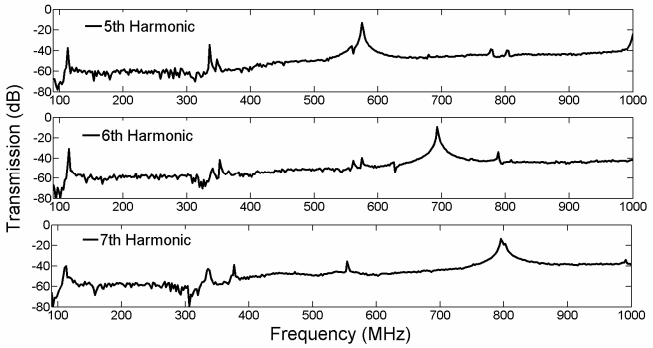

Figure 11. Measured transmission (S21) for the resonartors in Fig. 10 with interdigitated electrodes for selectively driving the resonator 5th, 6th, and 7th harmonics. The interdigitated electrodes suppress unwanted resonator harmonics by > 20 dB.

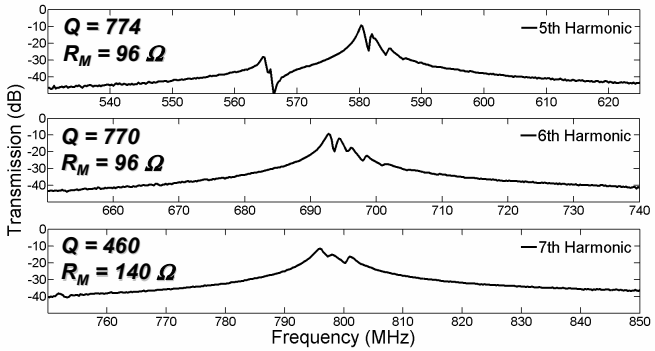

Figure 12. Close-in image of the resonant peaks in Fig. 11.

section III, indicate that the spurious modes can be reduced by anchoring in 4, rather than 2, locations on the ring. Using interdigitated electrodes to selectively transduce a resonator harmonic, the resonator frequency has been successfully scaled without increasing device size or impedance.

V. Piezoelectric Resonant Sensors

Post-CMOS compatible inertial, chemical, biological and other sensors are of great interest, where electronics integration allows for reduced microsystem size, lower power consumption and improved sensor sensitivity. An AlN resonant accelerometer based on DETF beams has been developed and is pictured in Fig. 13 with an SEM image of the accelerometer shown in Fig. 14. Table IV summarizes the dimensions of the resonant accelerometer. Resonant sensing techniques were chosen because of their high sensitivity, high dynamic range, and direct digital output, which eliminates the need for power hungry analog-to-digital converters. Resonant sensing improves the sensor sensitivity to low frequency inertial signals in this process because the piezoelectric effect is more pronounced at high frequencies. The electrode placement on top of the resonant sensing beams shown in Fig. 13(b) drives the device in the DETF mode. The DETF configuration reduces anchor loss and prevents the resonators from inducing a torque on the proof mass.

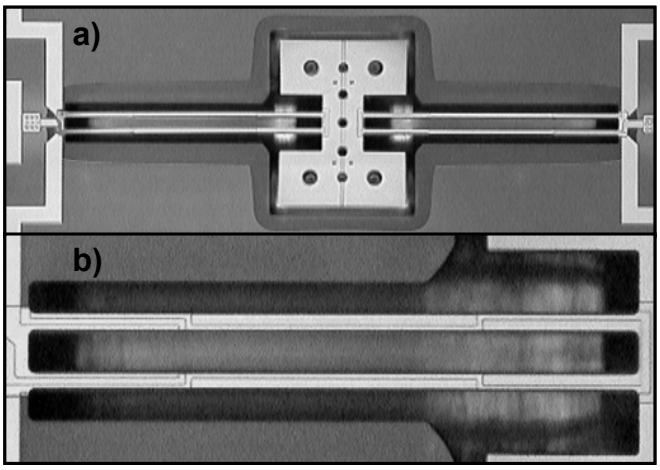

Figure 13. a) AlN resonant accelerometer. b) top electrode layout for transducing the DETF mode.

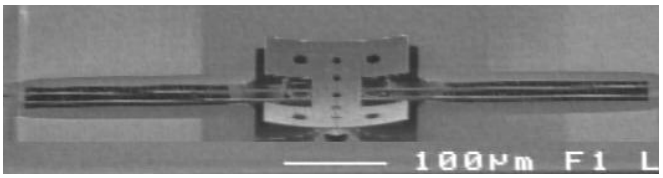

Figure 14. SEM image of the AlN resonant accelerometer.

TABLE IV. Resonant Accelerometer Dimensions

Accelerometer Parameter	Symbol	Value
DETF Length	*l*	300 µm
DETF Width	*w*	6 µm
Device Thickness	*t*	1.1 µm
Proof Mass	*m*	100 ng

A. DETF and Oscillator Readout Circuitry Performance

The transmission of the DETF sensing beams (Al bottom electrode) in Fig. 13 measured in vacuum is shown in Fig. 15. The resonant frequency is 727 kHz, the motional impedance is 2 MΩ and the Q is 2160. The 1 dB compression point for the DETF resonant sensing beams occurs at 1.4 Vpp (245 nW), leading to an improvement in the power handling when compared to beam resonators driven electrostatically via comb drives [10] or parallel plate actuators (82 nW) [11] which suffer from electrostatically induced Duffing distortion. Duffing nonlinearity is not the limiting mechanism in the power handling of the piezoelectrically driven DETF resonators. The circuit used to oscillate the DETF resonant sensing beams was modified from [12] and is shown in Fig. 16 with the measured oscillator output waveform shown in Fig. 17. The single sided phase noise power for the oscillator is shown in Fig. 18. Below 275 Hz the phase noise profile is $1/f^4$ while above 1100 Hz the measurement is limited by the noise floor of the spectrum analyzer. From 275-1100 Hz the phase noise is $1/f^3$ as predicted by [13]

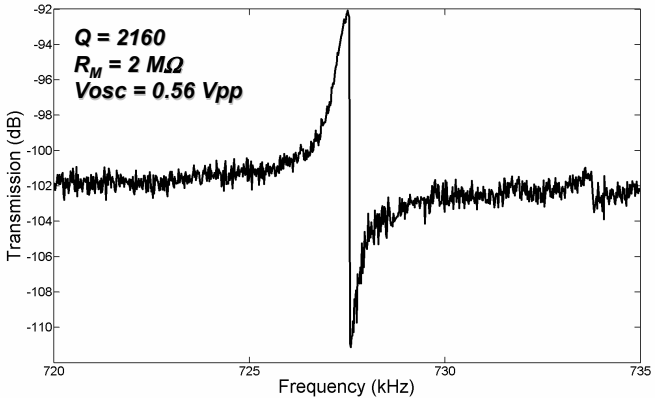

Figure 15. Measured transmission (S21) for the DETF resonant sensor shown in Fig. 13.

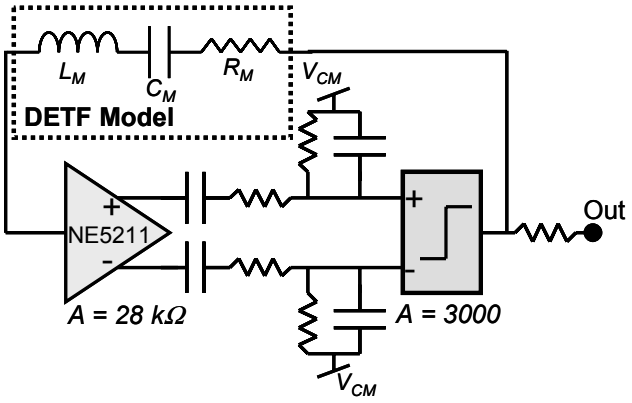

Figure 16. Oscillator readout circuit schematic for the DETF resonant sensing beams.

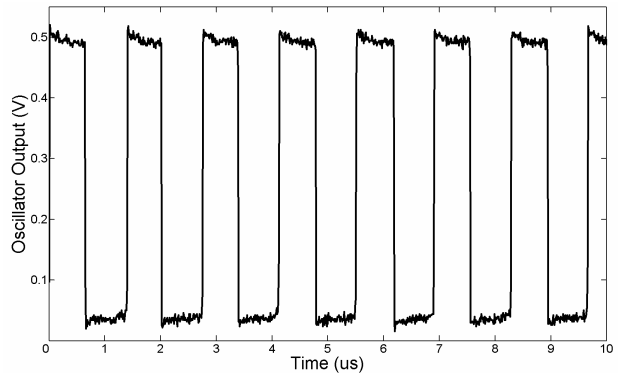

Figure 17. Output waveform of the DETF oscillator. The resistor in series with the output in Fig. 16 divides the output voltage by 10.

$$L(\Delta f) = 10\log\left[\frac{2KT}{P_{sig}}\left(\frac{f_0}{2Q\Delta f}\right)^2\right]. \quad (4)$$

However, the predicted phase noise given a Q of 2160, a motional impedance of 2 MΩ, and a 5 V square wave oscillator output (Psig = 5 μW) is -164 dBc/Hz at 1100 Hz offset from the carrier, which is 70 dBc lower than the measured value of -93.4 dBc/Hz. While a previous implementation of the circuit in Fig. 16 had 16 dB of increased phase noise in the *1/f²* region due to noise folding in the comparator [14], the measured results still have 54 dB excess noise than expected. Since

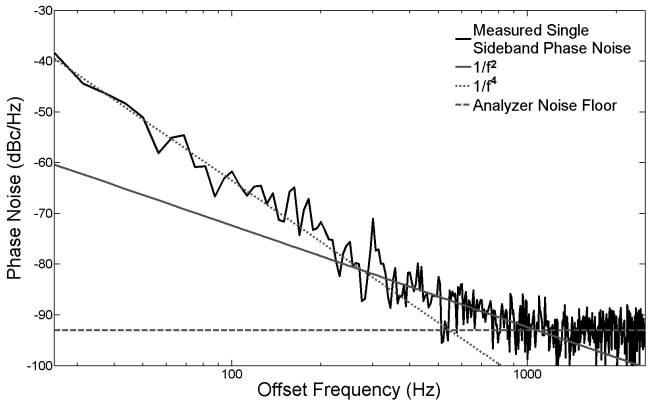

Figure 18. DETF oscillator single sided phase noise plot.

$$R_M \approx \frac{1}{Q}, \quad (5)$$

and

$$P_{sig} = \frac{\left(\frac{2V_{osc}}{\pi}\right)^2}{R_M} \approx Q\left(\frac{2V_{osc}}{\pi}\right)^2, \quad (6)$$

any reduction in the Q due to the circuitry overdriving the resonator degrades the phase noise by Q^3,

$$L(\Delta f) = 16 + 10\log\left[\frac{2KTQ_0}{P_{sig0}}\left(\frac{f_0}{2\Delta f}\right)^2\left(\frac{1}{Q_D}\right)^3\right] \quad (7)$$

where, $Q_0 = 2160$, $P_{sig0} = 5\,\mu W$, Q_D is the in-circuit Q accounting for any degradation and the additional 16 dB estimates the noise due to nonlinearities in the comparator [14]. Since the resonator is being driven by a comparator, it is unable to self limit [11] and driving the resonator beyond 1.4 Vpp can significantly degrade the Q. The measured results indicate that overdriving of the DETF resonant sensing beams by the 5 V comparator output is degrading the Q to approximately 32. A new linear circuit currently being designed that limits the resonator drive voltage to 1 Vpp has a predicted phase noise of -150 dBc/Hz at 1100 Hz offset from the carrier.

B. Accelerometer Performance

The sensitivity, *Γ*, of the DETF sensing beams to acceleration, *G*, is [7]

$$\Gamma = \frac{\frac{\Delta f}{f_0}}{G} = \frac{0.72ml^2}{Etw^3}, \quad (8)$$

where m is the weight of the proof mass and l, w, and t are the beam length, width and thickness, all given in Table IV. An acceleration, a, produces a phase noise sideband, L_v, at the frequency of vibration, f_v, offset from the carrier equal to [15]

$$L_v(\Delta f_v) = \left(\frac{\left|\vec{\Gamma}\right| f_0 \vec{a}(f_v))}{2 f_v} \right)^2 . \quad (9)$$

Thus the phase noise power due to vibration goes as $1/f_v^2$, giving a constant signal-to-noise ratio between 275 Hz and 1100 Hz where the phase noise power due to the oscillator also has a $1/f^2$ profile. The accelerometer sensitivity is

$$a_{\min}(f_v) = \frac{2 f_v \sqrt{L_{osc}(\Delta f_v)}}{\vec{\Gamma} f_0} . \quad (10)$$

The accelerometer in Fig. 13, with a proof mass of only 100 ng, achieves an acceleration sensitivity of 565 $mG_{RMS}/\sqrt{Hz}$ when coupled with the oscillator in Figs. 16 - 18. The acceleration sensitivity can be improved to 0.8 $mG/\sqrt{Hz}$ by reducing the readout oscillator phase noise as discussed above. In addition, increasing the size of the proof mass in Fig. 13 to 2 mm x 2 mm improves the acceleration sensitivity with the existing oscillator to 4 $mG/\sqrt{Hz}$ and with the proposed reduced noise oscillator to 6 $\mu G/\sqrt{Hz}$.

VI. Conculsions

Post-CMOS compatible AlN filters, resonators, and resonant sensors have been developed for microsystem miniaturization and expanded capabilities. A 2nd order, 0.5% bandwidth, 108.4 MHz dual mode band-pass filter has been realized occupying an area of 0.06 mm^2. The power handling of the filter is 7 dBm and the stopband rejection is greater than 55 dB. When terminated with 75 Ω, this filter achieves an insertion loss of 4.7 dB, a passband ripple of 1 dB and a 20 dB shape factor of 2.6. The bandwidth and center frequency of this dual mode filter are lithographically definable and a 5-element bank of 0.6% bandwidth filters have been demonstrated from 106 – 113 MHz. In order to scale AlN ring resonators to higher frequencies without subsequent increases in size or impedance, resonators selectively driven at the 5th, 6th, and 7th harmonic by interdigitated transducers have been demonstrated reaching frequencies of 796 MHz, impedances as low as 96 Ω and quality factors of 774 without increasing resonator size. The interdigitated electrodes reject unwanted resonator harmonics by greater than 20 dB. Double ended tuning fork resonant sensing beams have been developed in this process at 727 kHz with Q's of 2160 and motional impedances of 2 MΩ. A first generation readout circuit that oscillates the DETF resonators has been demonstrated achieving a phase noise of -81 dBc/Hz at 275 Hz offset from the carrier, 70 dB above the theoretical limit due to noise folding and overdriving of the DEFT sensing beams. The sensitivity of an accelerometer with a 100 ng proof mass occupying 0.15 mm^2 is 565 $mG/\sqrt{Hz}$ and can be improved to $4mG/\sqrt{Hz}$ by reducing the oscillator output power. Methods for scaling AlN resonant accelerometers to sub $10\mu G/\sqrt{Hz}$ by increasing the size of the proof mass have also been presented.

Acknowledgment

The authors would like to thank the Microelectronics Development Laboratory staff at Sandia National Laboratories including Jim Stevens, Mike Olewine and Pat Nelson for their contributions developing the AlN film. We would like to thank Chris Nordquist, Chris Dyck, Garth Kraus and Mark Ballance for use of their testing facilities and equipment and Kevin Smart for his guidance in the filter development. The contributions of Ken Pohl in assembling the oscillator circuitry is also very much appreciated.

References

[1] K. J. Smart, R. H. Olsson III, D. Ho, D. R. Heine, and J. G. Fleming, "Frequency agile radios using MEMS resonators," *Proc. of the Govt. Microcircuit App. and Critical Tech. Conf.*, pp. 409-412, March 2007.

[2] C. T.-C. Nguyen, "MEMS technology for timing and frequency control," *IEEE Trans. On Ultrasonics, Ferroelectrics, and Frequency Control,* vol. 54, no. 2, pp. 251-270, Feb. 2007.

[3] R. Ruby, P. Bradly, J. D. Larson III, and Y. Oshmyansky, "PCS 1900 MHz duplexer using thin film bulk acoustic resonators (FBARs)," *Electronics Letters,* vol. 35, no. 10, pp. 794-795, May 1999.

[4] G. Piazza, P. J. Stephanou, and A. P. Pisano, "Piezoelectric aluminum nitride vibrating contour-mode MEMS resonators," *Journal of Microelectromechanical Systems,* vol. 15, no. 6, pp 1406-1418, Dec. 2006.

[5] H. Chandrahalim, D. Weinstein, L. F. Cheow, and S. A. Bhave, "Channel-select micromechanical filters using high-K dielectrically transduced MEMS resonators," Proc. of the 19th *IEEE Int. Conf. Microelectrocmechanical Systems,* pp. 894-897, Jan. 2006.

[6] M. U. Demirci and C. T.-C. Nguyen, "Mechancially corner-coupled square microresonator array for reduced series motional resistance," *Journal of Microelectromechanical Systems,* vol. 15, no. 6, pp. 1419-1436, Dec. 2006.

[7] A. A. Seshia, et al., "A vacuum packaged surface micromachined resonant accelerometer," *Journal of Microelectromechanical Systems,* vol. 11, no. 6, pp. 784-793. Dec. 2002,

[8] P. J. Stephanou, G. Piazza, C. D. White, M. B. J. Wijesundara, and A. P. Pisano, "Piezoelectric thin film AlN annular dual contour mode bandpass filter," *Proc. ASME IMECE2005,* 2005.

[9] G. Piazza, P. J. Stephanou, and A. P. Pisano, "Single-chip multiple frequency ALN MEMS filters based on contour-mode piezoelectric resonators," *Journal of Microelectromechanical Systems,* vol. 16, no. 2, pp. 319-328, April 2007.

[10] C. T.-C. Nguyen and R. T. Howe, "An integrated CMOS micromechanical resonator high-Q oscillator," *IEEE Joural of Solid-State Circuits,* vol. 34, no. 4, pp. 440-455, April 1999.

[11] S. Lee and C. T.-C. Nguyen, "Influence of automatic level control on micromechanical oscillator phase noise," *Proc. 2003 IEEE Int. Frequency Control Symposium,* pp. 341-349, May 2003.

[12] K. E. Wojciechowski, B. E. Boser, and A. P. Pisano, "A MEMS resonant strain sensor operated in air," *Proc. 17th International IEEE Micro Electro Mechanical Conference*, pp. 841-845, Jan. 2004.

[13] T. H. Lee and A. Hajimiri, "Oscillator phase noise: A tutorial," *IEEE Journal of Solid-State Circuits,* vol. 35, no. 3, pp. 326-336, March 2000.

[14] K. E. Wojciechowski, "Electronics for resonant sensors," *Ph.D. Dissertation,* Dept. of EE and CS, Univ. of California, Berkeley, 2005.

[15] R. L. Filler, "The acceleration sensitivity of quartz crystal oscillators: A review," *IEEE Trans. on Ultrasonics, Ferroelectrics, and Frequency Control,* vol. 35, no. 3, May 1988.